A Bayesian approach to infer interior mass anomalies from the gravity data of celestial bodies

Kristel Izquierdo [ORCID], Vedran Lekić [ORCID] and Laurent G.J. Montési [ORCID]

Department of Geology, University of Maryland, College Park, MD 20782, USA. E-mail: kig@umd.edu

SUMMARY

Inversions of planetary gravity are aimed at constraining the mass distribution within a planet or moon. In many cases, constraints on the interior structure of the planet, such as the depth of density anomalies, must be assumed *a priori*, to reduce the non-uniqueness inherent in gravity inversions. Here, we propose an alternative approach that embraces the non-uniqueness of gravity inversions and provides a more complete view of related uncertainties. We developed a Transdimensional Hierarchical Bayesian (THB) inversion algorithm that provides an ensemble of mass distribution models compatible with the gravitational field of the body. Using this ensemble of models instead of only one, it is possible to quantify the range of interior parameters that produce a good fit to the gravity acceleration data. To represent the interior structure of the planet or moon, we parametrize mass excess or deficits with point masses. We test this method with synthetic data and, in each test, the algorithm is able to find models that fit the gravity data of the body very well. Three of the target or test models used contain only point mass anomalies. When all the point mass anomalies in the target model produce gravity anomalies of similar magnitudes and the signals from each anomaly are well separated, the algorithm recovers the correct location, number and magnitude of the point mass anomalies. When the gravity acceleration data of a model is produced mostly by a subset of the point mass anomalies in the target model, the algorithm only recovers the dominant anomalies. The fourth target model is composed of spherical caps representing lunar mass concentration (mascons) under major impact basins. The algorithm finds the correct location of the centre of the mascons but fails to find their correct outline or shape. Although the inversion results appear less sharp than the ones obtained by classical inversion methods, our THB algorithm provides an objective way to analyse the interior of planetary bodies that includes epistemic uncertainty.

Key words: Lunar and planetary geodesy and gravity; Inverse theory; Probability distributions; Statistical methods; Planetary interiors.

1 INTRODUCTION

The mass distribution inside the Earth is directly related to mantle upwellings, downwellings, dynamic tomography and plate motions (Hager & O'Connell 1981; Forte & Peltier 1987). Mapping it is key for constraining planet-scale dynamics. On Earth, seismic observations of normal modes can be used to infer large-scale density variations on their own (Moulik & Ekström 2016; Koelemeijer *et al.* 2017) or in combination with gravity data (e.g. Ishii & Tromp 1999), albeit with large uncertainty and trade-offs (Romanowicz 2001). On other planetary bodies, however, seismic data is scarce or non-existent (Lognonné 2005), but gravity data are relatively abundant. Gravity data have been sampled globally from orbiting spacecraft around the Moon (Konopliv *et al.* 2013), Mars (Genova *et al.* 2016), Mercury (Smith *et al.* 2012), Venus (Li *et al.* 2015) and other celestial bodies (Anderson *et al.* 2001; Iess *et al.* 2010;

Konopliv *et al.* 2018). With these data sets, gravity inversions have been performed to reveal local or global mass anomalies.

Inversions of the gravity field of the Moon have been particularly instructive. Inversion of data from the Gravity Recovery and Interior Laboratory (GRAIL) mission showed that the crust of the Moon is less dense, more porous, and thinner than previously thought (Wieczorek *et al.* 2013). This result brought estimates of lunar composition closer to those implied by the giant impact hypothesis for the Moon's formation. Gradiometry from the same data revealed elongated positive density anomalies on the surface. Their size, orientation and distribution were interpreted as dikes resulting from the expansion of the young Moon (Andrews-Hanna *et al.* 2013) and rifts from differential contraction between the Procellarum region and surrounding terrains (Andrews-Hanna *et al.* 2014). Many other gravity studies have provided insights on the Moon's subsurface (Andrews-Hanna 2013; Melosh *et al.* 2013b; Besserer *et al.* 2014;

Miljković *et al.* 2015; Gong *et al.* 2016; Soderblom *et al.* 2016; Jansen *et al.* 2017) and on the subsurface of other celestial bodies (Beuthe *et al.* 2012; Konopliv *et al.* 2014; Goossens *et al.* 2017).

Despite these successes, using gravity data to infer density anomalies is difficult due to the inherent non-uniqueness of gravity inversions (Backus & Gilbert 1967; Li & Oldenburg 1998), specially if the depth of these anomalies is not constrained by other observations. Gravity inversions in (Liang *et al.* 2014; Zhao *et al.* 2019) have provided estimates of the excess mass of uplifted mantle beneath Maries by applying a radial weighting function that constrains the radial distribution of anomalies. Although this eliminates the need of additional observations constraining the depth of anomalies, the resulting radial density distribution is dependent on the weighting function chosen. Since a group of density distributions can fit the data with the same error, it is necessary to show all fitting models in order to understand the variations in the density distribution can produce the observed gravity data. This representation of the variations in the resulting density distribution is missing in 3-D gravity inversions to date.

The non-uniqueness of gravity inversions should be quantified as part of the epistemic uncertainty in resulting mass distribution models. This non-uniqueness might cause different mass distributions to fit the gravity acceleration data with the same error leading to a much higher variability between models than due solely to aleatory errors in the measurements of gravitational acceleration. Another source of epistemic uncertainty is the representation of mass anomalies in a model. The mass anomalies actually present in a planetary body probably form complex shapes. These shapes may be simplified in models in different ways, including point masses, spherical caps and tesseroids. Gravity inversion results are typically evaluated by how well they fit an input gravity field, but how well they fit the actual interior density distribution depends also on epistemic uncertainty and is therefore more uncertain.

A Transdimensional Hierarchical Bayesian (THB) approach to the inversion of gravity data provides a framework for exploring uncertainties related to gravity inversions (Sambridge *et al.* 2006). With the THB approach, it is possible to sample the *a posteriori* probability distribution of models given the data and constraints based on prior information, in a way that is flexible and does not require—but can accommodate—prior assumptions concerning the complexity and location of mass anomalies. Therefore, the results of THB inversions are not represented by a single model but, instead, by an ensemble of models that fit the data. We find it convenient to summarize this ensemble of models by: (1) the average value of each parameters of the interior mass distribution model and (2) the range of values for those parameters where there is a 1σ or $n\sigma$ confidence that the true value lies. Access to the entire ensemble, though, allows a more complete view of all possible solutions, including trade-offs and correlations between parameter values. This more complete quantification of uncertainty in gravity inversions enables a better grasp of the implications of retrieved structures.

In gravity inversions to date, the use of a Transdimensional Bayesian algorithm has been limited to the recovery of 2-D local-scale density structures. The shape of a 2-D polygon, defined by a fixed density difference and size, a varying number of vertices in the *x–y* plane and an infinite length in the *z*-direction, can be recovered (Luo 2010). In Titus *et al.* (2017), the additional parameters of density difference and size of a rectangle containing the polygon were also estimated.

In this paper, we present a THB gravity inversion algorithm designed to recover an ensemble of mass distribution models of a spherical body from gravity acceleration data which is the radial derivative of the gravitational potential. The number of parameters is not fixed *a priori* (transdimensional aspect) but instead chosen in light of the data. The variance in the data is also estimated as part of the inversion technique (hierachical aspect). In Section 2, we describe the Bayesian approach and the general logic of the algorithm. In Section 3, we show the results of inverting several synthetic gravity fields to illustrate the capabilities and limitations of the method.

2 INVERSION TECHNIQUE

In this section, we describe how Bayes' rule is used to assign probabilities to different mass distributions inside a sphere when the number of parameters is not fixed *a priori*. We also present the reversible jump Markov chain Monte Carlo (rjMcMC) algorithm (Green 1995) used to perform THB gravity inversions. We will use brackets {} to represent sets of values for one parameter, such as the value of each anomaly in the model {m}, or the gravity acceleration data, {g}. Since {g} is only informative to the inversion when the effect expected from a sphere of constant density is removed, the terms gravity acceleration data or gravity anomaly might be used to refer to {g}.

2.1 Bayesian inference

Bayes' rule states that the probability P of having an interior mass anomaly with magnitude m given the gravity acceleration values at the surface {g} is proportional to the probability of observing {g} if the mass anomaly is m multiplied by the probability of the mass anomaly being m according to our current understanding of its possible values: $P(m|\{g\}) \propto P(\{g\}|m)P(m)$. $P(m|\{g\})$ is formally known as the posterior probability function, $P(\{g\}|m)$ as the likelihood and $P(m)$ is the prior.

2.2 Transdimensionality

In the classical use of Bayesian inference, the number of mass anomalies n in the model was fixed. In the case described above, it was set to one. Thus m was a scalar. If the number of mass anomalies is not known *a priori*, n can be treated as another parameter to invert from data {g}. Eq. (1) shows the updated probability distribution function $P(\{m\}, n|\{g\})$.

$$P(\{m\}, n|\{g\}) \propto P(\{g\}|\{m\}, n)P(\{m\}, n). \tag{1}$$

There are now $n + 1$ unknowns to be determined. A transdimensional inversion provides the added flexibility of estimating the number of layers in a 2-D velocity model using seismic data, for example, or the number of density anomaly objects in a 3-D model using gravity data. This flexibility is required because we do not actually have that information when working with real data, since the anomalies lie in the inaccessible interior of the planet.

2.3 Reversible jump Markov chain Monte Carlo algorithm (rjMcMC)

We represent the mass anomalies inside a sphere with point masses. We describe in Section 3.2.4 how this parametrization performs when the gravity data to invert is produced by finite-sized objects instead of point masses. Using this parametrization, the interior

mass distribution model $\{p_m\}$ contains the values of each parameter describing the mass distribution in the interior of the sphere: $\{p_m\} = \left\{n, \{m\}, \{x\}, \{y\}, \{z\}, \sigma_g^2\right\}$ where n is the number of point mass anomalies, $\{m\}$ is the set of values of the mass anomalies in kilograms, $\{x\}$, $\{y\}$ and $\{z\}$ are their Cartesian coordinates in kilometers and σ_g^2 is the variance of the white noise of the gravity acceleration data in $(\mathrm{m\,s}^{-2})^2$. The corresponding posterior probability implied by Bayes' theorem in eq. (2) is:

$$
\begin{aligned}
P(\{p_m\}|\{g\}) &= P(n, \{m\}, \{x\}, \{y\}, \{z\}, \sigma_g^2|\{g\}) \\
&\propto P(\{g\}|\{p_m\})P(\{p_m\})
\end{aligned} \quad (2)
$$

with the likelihood $P(\{g\}|\{p_m\})$ given by:

$$
P(\{g\}|\{p_m\}) = \frac{1}{\sqrt{2\pi^n \left(\sigma_g^2\right)^s}} \exp\left(-\frac{\Phi}{2}\right), \quad (3)
$$

where s is the number of independent observation points and

$$
\Phi = (\{g\} - \{g_M\})^T \frac{1}{\sigma_g^2}(\{g\} - \{g_M\}), \quad (4)
$$

where $\{g_M\}$ are gravity accelerations predicted by model $\{p_m\}$.

Using the Metropolis–Hastings criteria (Hastings 1970), we construct an algorithm that finds the values $n, \{m\}, \{x\}, \{y\}, \{z\}, \sigma_g^2$ that best fits the data and additional constraints in an unbiased way. The process to do this is divided in two steps: (1) proposing models from the distribution $q(\{p'_m\}|\{p_m\})$ and (2) accepting models with the probability given by eq. (5).

$$
\alpha(\{p'_m\}|\{p_m\}) = \min\left[1, \frac{P(\{p'_m\})P(\{g\}|\{p'_m\})}{P(\{p_m\})P(\{g\}|\{p_m\})} \frac{q(\{p_m\}|\{p'_m\})}{q(\{p'_m\}|\{p_m\})}\right]. \quad (5)
$$

The expressions for the proposal distributions and derivation are presented in Appendix A. When adding a new anomaly, its parameters are taken from the prior distributions which are uniform. When changing the location of an existing anomaly, the new location is selected from a normal distribution with mean at the current location.

Fig. 1 shows a detailed flowchart of the algorithm. At each step of the rjMcMC, we propose a random new model based on perturbing the existing model. We either remove or change the location of a randomly selected anomaly, or we introduce a new anomaly with a location sampled randomly from the prior, or we perturb the variance describing the noise in the data.

It is important to note that after randomly choosing the location of the anomalies, we compute their corresponding masses by minimizing the difference between the predicted and observed acceleration values. This is possible thanks to the linear relation between the magnitude of a point mass and the acceleration it produces: $\{g\} = D\{m\}$. Here, D is a matrix constructed using the gravitational constant G and inverse of the distances between the point masses and the sampling points, d_{ij}, where i is the index of the mass considered and j is the index of the observation point: $D_{ij} = G/d_{ij}^2$. The optimal value of the point masses are determined in a least squares sense: $\{m_o\} = (D^T C_g^{-1} D)^{-1} D^T C_g^{-1} \{g\}$. Because uncertainty on the data $\{g\}$ are assumed to be normally distributed, $P(\{g\}|\{p_m\})$ will be represented by a generalized Gaussian with mean $\{m_o\}$ and posterior covariance given by $\tilde{C}_m = (D^t C_g^{-1} D + C_m^{-1})^{-1}$ (Tarantola 2005), where C_g is the data covariance matrix ($C_g = \sigma_g^2 I$) and C_m is the prior model covariance matrix. We set C_m to be a diagonal matrix since masses of individual anomalies are not assumed to be correlated *a priori*. The prior model covariance matrix also acts to stabilize the inversion for $\{m\}$ by contributing to the diagonal.

The advantage of solving for the optimal set of mass anomalies $\{m\}$ at each step of the rjMcMC is that doing so reduces by $\{n\}$ the dimensionality of the inverse problem, which dramatically improves the efficiency of the search, as we only have to explore a fraction of the model space. However, this also means that instead of obtaining the likelihoods of randomly generated models at each step of the rjMcMC (which is commonly the case), we only obtain the likelihoods for randomly generated models in which the values $\{m\}$ have been tuned to optimal values $\{m_o\}$ so that:

$$
P(\{g\}|\{p_{m_o}\}) = \max_{\{m\}} P(\{g\}|\{p_m\}). \quad (6)
$$

The presence of tunable parameters means that we cannot simply use the ratio of likelihoods when computing acceptance probabilities in eq. (5). Instead, it is necessary to marginalize over the set of tunable parameters $\{m\}$ prior to comparing likelihoods and deciding to accept or reject a proposed model. The marginalization removes the dependence on the tunable parameters:

$$
\begin{aligned}
P(\{g\}|n, \{x\}, \{y\}, \{z\}, \sigma_g^2) &= \int_{m_{\min}}^{m_{\max}} P(\{g\}|\{p_m\})P\{m\}d\{m\} \\
&= \frac{\sqrt{(2\pi)^n |\tilde{C}_m|}}{(m_{\max} - m_{\min})^n} P(\{g\}|\{p_{m_o}\}). \quad (7)
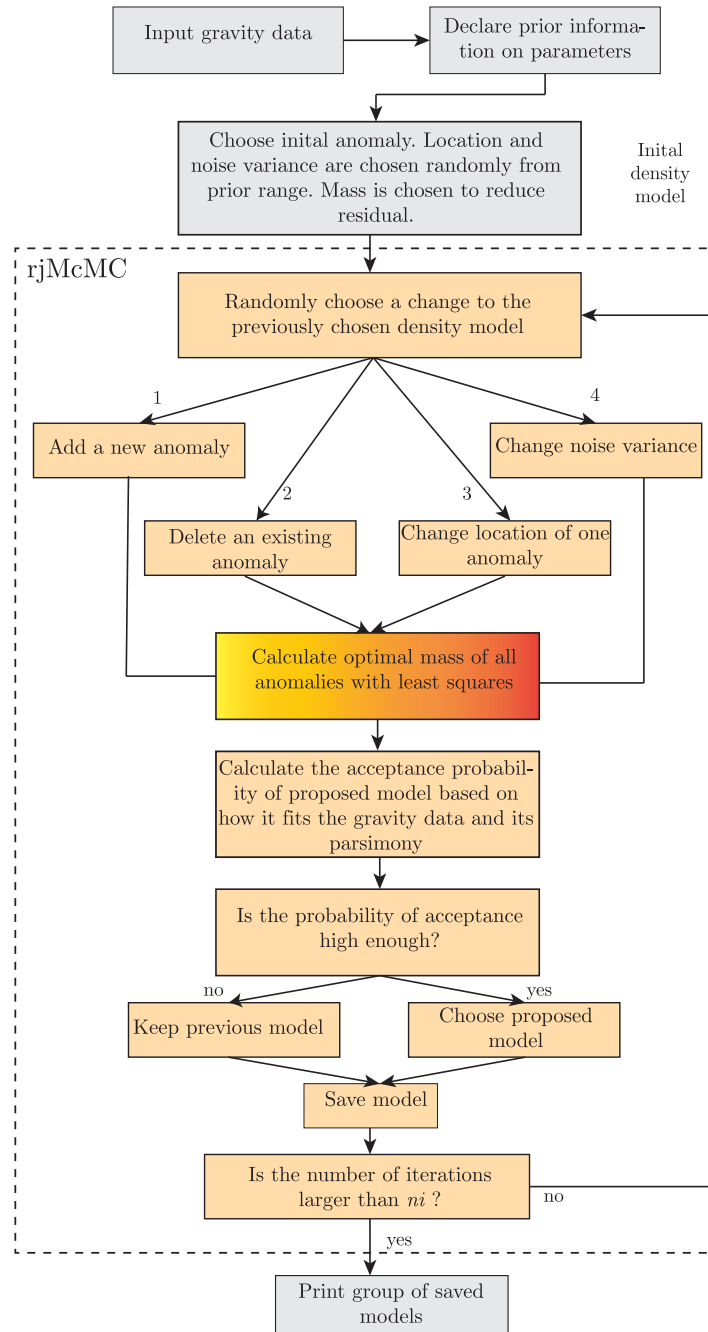\end{aligned}
$$

Putting this all together, the acceptance probability α used by the algorithm becomes:

$$
\begin{aligned}
\alpha = \min\Bigg[&1, \left(\frac{\sigma_g^2}{\sigma_g^{2\prime}}\right)^s \exp\left(-\frac{\Phi - \Phi'}{2}\right) \\
&\times \sqrt{\frac{|\tilde{C}_{m'}|}{|\tilde{C}_m|}}(m_{\max} - m_{\min})^{n-n'}\Bigg]. \quad (8)
\end{aligned}
$$

Since the optimal values of the anomalies is obtained by linear inversion, there is not a strict limit on its minimum and maximum possible values ($m_{\min}$ and $m_{\max}$). We use instead -10^{22} to 10^{22} kg as a sufficiently wide range in eq. (8).

2.4 Hierarchical parameter

As described above, our algorithm treats the uncertainty of the data, parametrized by the variance of the normal distribution describing white noise in the data (σ_g^2), as a parameter to be inferred during the inversion. This formulation is referred to as hierarchical (Malinverno & Briggs 2004). Since the complexity of the mass distribution models obtained by the algorithm depends on the level of noise in the data, it is important to estimate the noise variance together with the estimation of the values of the model parameters (Bodin *et al.* 2012). Inversions of data with higher noise levels should produce simpler models. Lower noise levels produce more complex models since a greater number of model parameters can be justified when attempting to fit the data. Even when the noise variance is estimated by external methods, like measurement uncertainties from satellite tracking data, estimating the hierarchical noise parameter through the inversion can be important in assessing how well the model can fit the data (epistemic uncertainty). For example, Olugboji *et al.* (2017) found that when constructing surface wave phase velocity maps, the hierarchical noise estimates are systematically higher than reported data uncertainties, and attributed the difference to additional uncertainty arising from modelling assumptions. Gao & Lekić (2018) detail how the parametrization of the model itself can degrade or bias inferences obtained by transdimensional Bayesian

Figure 1. Flowchart of the THB gravity inversion algorithm. The initial model is chosen randomly from the prior distribution and subsequent models are obtained from the current model either by changing the position of a randomly chosen anomaly, by changing the noise variance, or by adding a new or removing an existing anomaly according to the reversible jump Markov chain Monte Carlo (rjMcMC) procedure. Proposed models are accepted or rejected based on their relative likelihood (eq. 6). After a burn-in period, models are saved to the ensemble, which represents a sample of the posterior distribution $P(\{p_m\}|\{g\})$. Note that masses of the anomalies are not explored, but rather inverted for at each step of the algorithm.

inversion; we later discuss how these effects manifest in the hierarchical noise parameter in our inversions. In this paper, the level of noise is unknown but it is assumed to have a normal distribution.

3 VALIDATION

In order to assess the ability of the proposed method to characterize the mass anomaly distribution within a celestial object, we carry out

a suite of validation tests. We construct four different mass distributions by specifying the location and magnitude of mass anomalies inside a sphere with radius R and zero mean density. We call these mass distributions target or true mass distributions. We calculate the gravity acceleration produced by each target distribution and apply a level of white noise to it. The inversion algorithm described in Section 2 uses this synthetic gravity data as input to obtain a mass distribution ensemble. We then compare the mean of the ensemble with the corresponding target model to see how effectively the

Figure 1. Flowchart of the THB gravity inversion algorithm. The initial model is chosen randomly from the prior distribution and subsequent models are obtained from the current model either by changing the position of a randomly chosen anomaly, by changing the noise variance, or by adding a new or removing an existing anomaly according to the reversible jump Markov chain Monte Carlo (rjMcMC) procedure. Proposed models are accepted or rejected based on their relative likelihood (eq. 6). After a burn-in period, models are saved to the ensemble, which represents a sample of the posterior distribution $P(\{p_m\}|\{g\})$. Note that masses of the anomalies are not explored, but rather inverted for at each step of the algorithm.

inversion; we later discuss how these effects manifest in the hierarchical noise parameter in our inversions. In this paper, the level of noise is unknown but it is assumed to have a normal distribution.

3 VALIDATION

In order to assess the ability of the proposed method to characterize the mass anomaly distribution within a celestial object, we carry out

a suite of validation tests. We construct four different mass distributions by specifying the location and magnitude of mass anomalies inside a sphere with radius R and zero mean density. We call these mass distributions target or true mass distributions. We calculate the gravity acceleration produced by each target distribution and apply a level of white noise to it. The inversion algorithm described in Section 2 uses this synthetic gravity data as input to obtain a mass distribution ensemble. We then compare the mean of the ensemble with the corresponding target model to see how effectively the

Table 1. Prior distributions of parameters used by the rjMcMC algorithm. R is the radius of the sphere. The limits of x, y and z are clearly marked by the boundaries of the sphere since anomalies cannot be outside it. The distributions of σ_g^2 and n do not have tangible limits. We instead set them to sufficiently large values so that the posterior distributions for these parameters are not truncated. In other words, the possible ranges of values are wide enough not to bias the search of the rjMcMC.

	x	y	z	σ_g^2	n
Min	$-R$	$-R$	$-R$	10^{-14} (m s^{-2})^2	1
Max	R	R	R	10^{-10} (m s^{-2})^2	140

algorithm recovered the mass distribution that produced the input gravity data.

The validation tests are divided in two types according to whether the mass anomalies of the target models are point masses or 3-D objects. Since the algorithm uses point masses to construct an output mass distribution, the goal is to test how well the algorithm recovers the location and magnitude of anomalies with a perfect parametrization and how it approximates the shape of finite objects with point masses.

3.1 Point masses as the target mass distribution model

In the first series of validations tests, the target mass distribution is built using point mass anomalies. It might be expected that the inversion algorithm, which parametrizes mass anomalies as point masses, should be able to recover the distribution perfectly. However, the resolution of the gravity data and the natural attenuation of $1/r^2$ of the gravity acceleration limit the combination of depths and magnitudes it can recover. In addition, the transdimensional aspect of the inversion method is inherently parsimonious, so the output distribution is likely to contain fewer mass anomalies than the target model.

We consider three cases in this category of target models. Target Model I and Target Model II contains five point mass anomalies (Table 2). In Target Model I, the deeper anomalies have larger magnitudes than the shallower anomalies and all the anomalies have different latitudes and longitudes. In Target Model II all the mass anomalies have the same latitude, longitude and mass but different depths. Target Model III contains 50 anomalies. Their locations and magnitudes are chosen from an uniform probability (see Supporting Information).

The parameters to recover are $\{m\}$, $\{x\}$, $\{y\}$, $\{z\}$, n and σ_g^2. The prior information given to the algorithm is shown in Table 1 with the only additional constraint that anomalies should be located inside the sphere $(x^2 + y^2 + z^2 \leq R^2)$. All inversions ran for 1×10^6 steps using only one McMC chain. Fig. 3 shows the log(likelihood) per step for the three cases. The likelihood increases with increasing number of steps or iterations of the algorithm until it stabilizes around iteration 4×10^5. The results shown next are taken from the group of models obtained after that step.

3.1.1 Fit to input gravity data

Fig. 2 shows the input gravity acceleration data used for each validation test and the gravity acceleration data of the mass distribution found by the algorithm. Each data set contains 2542 acceleration values uniformly sampled across the surface of the sphere. In case I, the gravity signature of each of the five point mass anomalies are clearly distinguished because larger magnitude deeper point masses

produce gravity signatures of similar amplitude as the smaller but shallower point masses and because all the point mass anomalies are positioned at different latitude and longitude. At first sight, it would appear that target model II has a gravity anomaly only at one location. That is because the five input masses have the same latitude, longitude and magnitude but different depths. Deeper anomalies with the same magnitude produce a broader and weaker gravity signal than shallower ones. In case III, the gravity data is produced by 50 point mass anomalies with random locations and magnitudes. For visualization, the gravity maps in Fig. 2 III are saturated at 250 mGal in order to show the gravity signatures of many anomalies. In reality, the shallowest mass anomaly produces a gravity acceleration as strong as 1000 mGal that dominates the gravity map, overpowering the other signals.

In all three cases, our inversion algorithm is able to find a mass distribution that fits the input gravity data. Additionally, the noise of the input gravity accelerations σ_g is recovered to 2 per cent error of the true value. However, the purpose of the inversion is not just to reproduce the input gravity values but to constrain the source. We discuss next the distribution of mass anomalies in the output model and how they compare with the target distribution.

3.1.2 Fit to target density model

As gravity inversions are non-unique, fitting the input gravity data does not mean the algorithm has found the correct mass distribution. In this section, we compare the mean of the model ensemble obtained by the algorithm with the known correct mass distribution (target model). In order to do that, we examine the posterior probability distribution of the models, $P(\{p_m\}|\{g\}) = P(n, \{m\}, \{x\}, \{y\}, \{z\}, \sigma_g^2|\{g\})$. Which shows the most likely combination of parameters given the gravity data. This posterior probability is obtained by measuring the frequency of different values of parameters from an ensemble of models obtained by the algorithm. The ensemble only contains models sampled after convergence is achieved. In other words, the sampling starts only after the residual between model prediction and input data (eq. 4) no longer changes significantly compared to the variation in the first set of iterations.

The locations of the gravity anomalies in the output acceleration data match those of the input (Fig. 2). This shows that density anomalies found by the algorithm are present at the correct latitudes and longitudes. Therefore, we focus on describing the distribution of the parameters that have trade-offs in gravity inversions: the magnitude and depth of anomalies.

Fig. 4 shows the comparison between the target and output models for test cases I, II and III. In test case I, there is perfect agreement between the mass anomalies in the target model and the inversion result. This shows that the algorithm is able to find the correct distribution of mass anomalies inside the sphere with non-informative priors for the situations when the gravity signature of the masses are equally dominant. In a more graphical way, this means that we can easily identify the signature of all masses in the gravity map (Fig. 2 I). Similarly, perfect matches were obtained for target models with n from 1 to 20 as long as each gravity signature was easily identifiable.

For case II, the algorithm fails to match the correct distribution. Instead, it finds a distribution that fits the gravity data using fewer point mass anomalies. As shown in Fig. 4(case II), the target model has five mass anomalies of the same magnitude (1×10^{16} kg) but different depths. Deeper mass anomalies produce very low magnitude gravitational acceleration compared to the shallower one which

Table 2. Location, number and magnitude of point masses used in Target Models I and II.

Parameter		Target Model I					Target Model II				
		1	2	3	4	5	1	2	3	4	5
Latitude (°)	θ	31.7	43.9	22.0	15.0	-65.9	-15.2	-15.2	-15.2	-15.2	-15.2
Longitude (°)	λ	-90	12.8	155.5	-63.3	-168.3	-80.3	-80.3	-80.3	-80.3	-80.3
Radius (R)	r	0.99	0.90	0.80	0.70	0.60	0.99	0.96	0.93	0.90	0.87
Mass (kg)	m	10^{16}	10^{18}	2×10^{18}	5×10^{18}	9×10^{18}	10^{16}	10^{16}	10^{16}	10^{16}	10^{16}
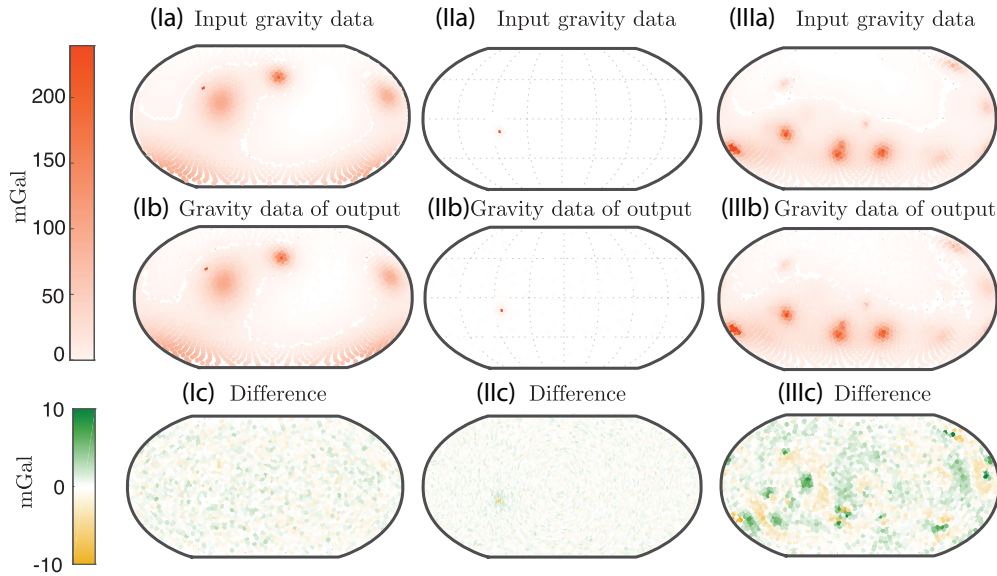
Figure 2. Gravity acceleration data used as input in the inversion (a) and gravity acceleration data produced by the output which is the mean of the ensemble of mass distribution models (b). In the three cases shown here, the target model consists of point masses. Target model 1: five point masses with different depths and magnitudes. Target model II: five point masses with the same latitude and longitude but different depths. Target model III: fifty point masses with random locations and magnitudes. The maximum misfit magnitude is 10 mGal in places where the acceleration is 200 mGal or higher, as shown by maps in (c), indicating that the algorithm is able to provide satisfactory data fits. Figures III (a) and III (b) are saturated to 200 mGal to show the gravity signal produced by several point masses. Otherwise the maps are dominated by the signal of one very large and shallow point mass. Tables B1 and B2 in the supplementary material provide the locations and magnitudes of all 50 point masses.
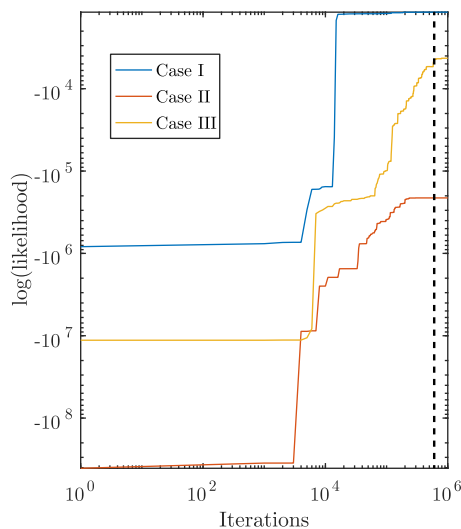

Figure 3. Likelihood plots for cases I, II and III. We can see that the likelihood increases with the number of iterations until it reaches a higher value where it stabilizes. The ensembles are composed of models from the 4×10^5 to the 1×10^6 iteration.

causes the fit of the model to the data to be dominated by one shallowest mass. As can be seen in eq. (8) in the term $(m_{\max} - m_{\min})^{n-n'}$ where n is the number of point masses, the THB algorithm prefers models with fewer anomalies, which means that it tends to match the gravity signature of the dominant anomalies only. Here the algorithm favours a single anomaly with a larger magnitude in a shallow location instead of the correct location of the five anomalies. The deeper mass anomalies in the target model produce subtle gravity signatures that are considered noise by our inversion algorithm. A lower noise variance (σ_g^2) would enhance the significance of weak features of the input gravity data, and would therefore justify the placement of additional anomalies.

For test case III, something similar to test case II occurs. In Fig. 4(case III), we can see that the mass anomalies located in the upper right triangle of the plot r versus m are preferentially recovered by the algorithm. This means that, again, the algorithm is less sensitive to the presence of deeper, smaller masses that do not contribute much to the residual. Reflecting its inherent parsimony, the algorithm fits the gravity data with fewer masses than present in the target model. Fig. 5 shows the number of anomalies recovered by the THB method in comparison with the ones contained in the true or target models of test cases I, II and III.

In summary, the algorithm is able to find mass distribution models that fit the input gravity data and accurately recovers the input noise
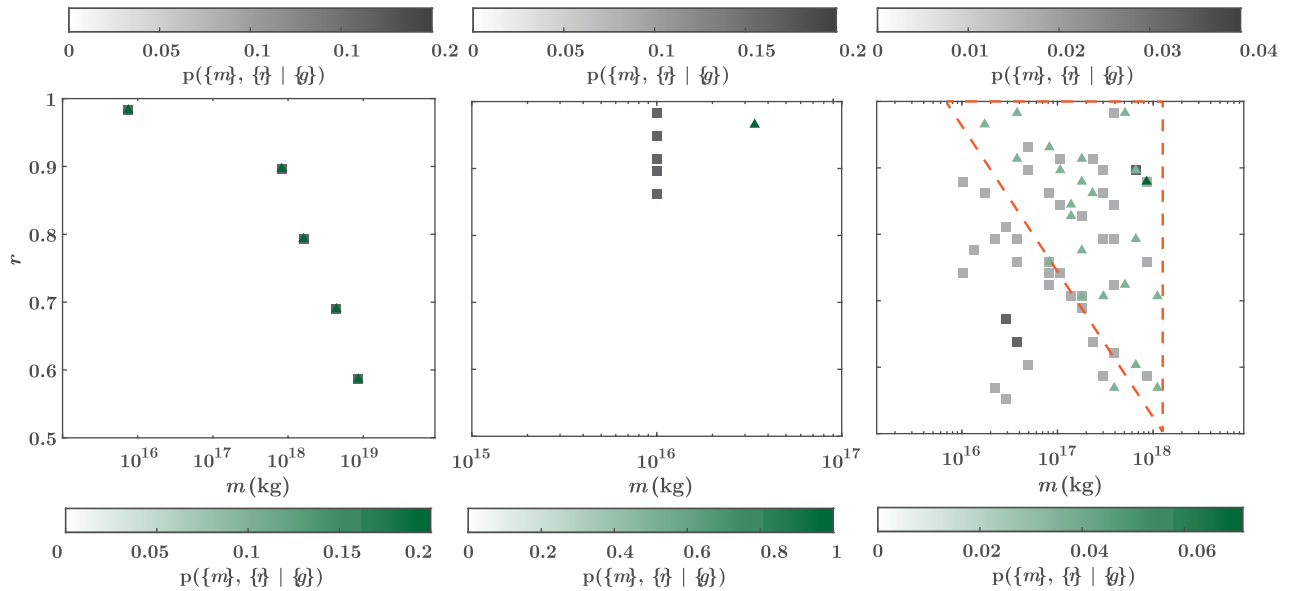
Figure 4. Comparison of target mass anomalies (squares) with output mass anomalies (triangles) and associated probability distributions for cases I, II and III. The location of the symbol shows the magnitude of a point mass and its distance from the centre of the sphere. The colour shows the probability of having a point mass there based on the input gravity acceleration data. In case I there is perfect agreement between the output and target models and between the probability distributions. In case II the inversion favours a single point mass anomaly of larger magnitude than the five point mass anomalies in the target model. The point mass anomalies in output model III have shallower locations or larger magnitudes. The red triangle is included to highlight this fact. Point mass anomalies outside this triangle appear in the target model but not in the output one. This mismatch happens because the algorithm is parsimonious and uses the fewer number of total anomalies possible. Deep and small anomalies do not affect the residual as strongly as shallow and large ones, so the parsimony of the algorithm works against their recovery.
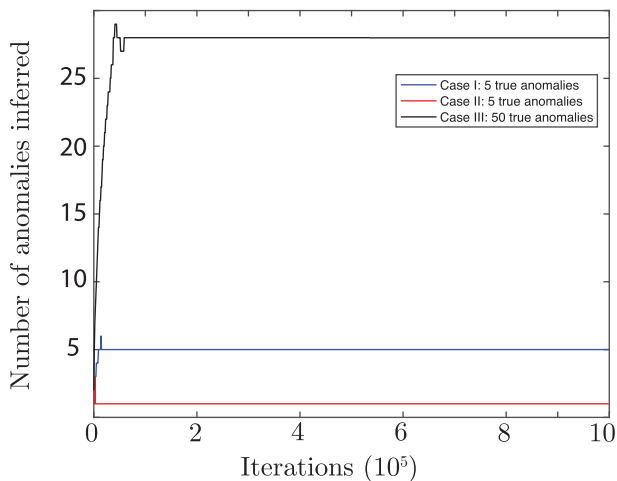
Figure 5. Number of anomalies inferred by the THB algorithm. For case I, the correct number of anomalies is found, while for cases II and III, fewer anomalies are recovered. This is a reflection of the parsimony of the algorithm. Since some deep and small anomalies do not substantially affect the residual (defined by eq. 4), and the algorithm prefers simpler to more complex models (i.e. it is parsimonious), the algorithm does not introduce these masses when fitting the input gravity acceleration data.

levels. However, in all three cases, the inherent parsimony of the method makes it difficult to recover all the anomalies when a subset of them dominate the gravity data and overpower the contributions of smaller and/or deeper masses to the residual. Lower input noise levels would justify the introduction of additional point masses. This behavior is common in all transdimensional inversions where the number of seismic velocity layers or density anomaly objects is

not specified *a priori* (e.g. number of layers recovered in transdimensional Bayesian surface wave dispersion Gao & Lekić 2018). Although it might be tempting to fix the number of parameters in order to avoid this problem in the tests presented here, that approach is not appropriate for the study of real gravity data sets, where the number of density anomalies is not known *a priori*. Instead, it is important to understand the limitations of transdimensional inversions and interpret the results taking this limitations into account.

### 3.2 Spherical caps as the target density model

As a second set of validations tests, we invert a set of gravitational acceleration values that was produced by 3-D objects instead of point masses. It is necessary to see which features of our target 3-D objects we can recover using point masses. If necessary, future algorithm development may use a model parametrization with finite sized objects to recover target 3-D objects. The objects used here are similar in shape to the expected mass anomalies found under major impact basins on the Moon, called mascons (Melosh *et al.* 2013a). These objects are represented by spherical caps such as the one shown in Fig. 6.

3.2.1 Fit to input gravity data

We use synthetic gravity acceleration data that provides a simpler, idealized view of the lunar gravity field (Lemoine *et al.* 2013). This radial gravity acceleration map (Fig. 7a) was obtained by computing the radial gravity acceleration produced by spherical caps with sizes, latitudes and longitudes listed in Table 3. The location and size of these caps are similar to those of major basins on the Moon where large mass concentrations, called mascons, where identified (Muller & Sjogren 1968; Neumann *et al.* 1996). The outer shells of the caps
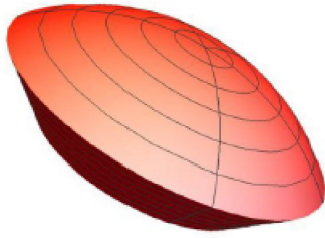
Figure 6. Spherical caps used as mass anomaly objects in the target model. They represent the volume inside a spherical shell of certain thickness $R_{max} - R_{min}$ limited by a concentric cone of aperture α.
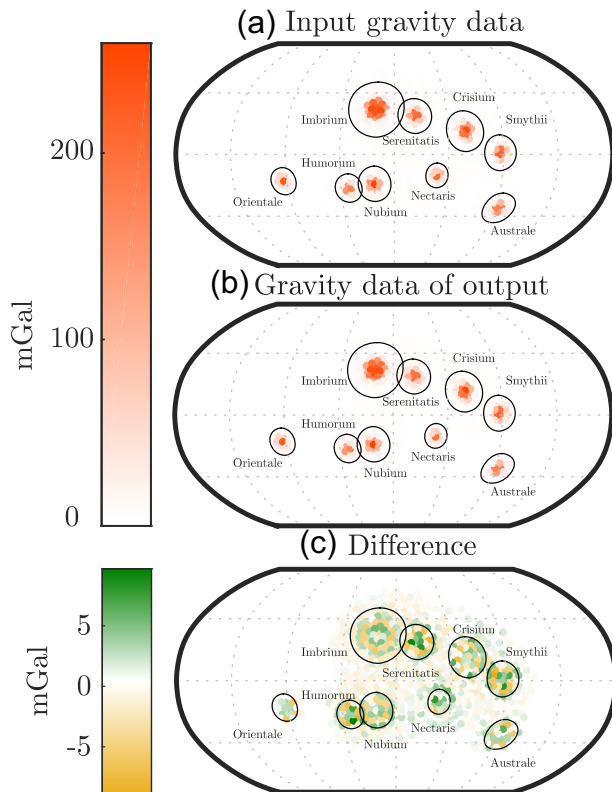
Figure 7. Comparison between the gravity data used as input in the inversion (a) and the gravity data produced by the mass distribution model found by the algorithm (b). The maps of differences (c) show that the error is only 5 mGal in places with a gravity acceleration larger than 200 mGal.

Table 3. Location and diameter of lunar basins used to produce the synthetic gravity data. The density anomaly of these mascons is 300 kg m^{-3}.

Name	Latitude	Longitude	Diameter (km)	Aperture (°)
Imbrium	32.8°N	15.6°W	224	23.21
Nubium	21.3°S	16.6°W	143	14.82
Serenitatis	28°N	17.5°E	141	14.61
Australe	38.9°S	93°E	120	12.44
Crisium	17°N	59.1°E	165	17.10
Humorum	24.4°S	38.6°W	115	11.92
Smythii	1.3°N	87.5°E	145	15.03
Nectaris	15.2°S	25.5°E	100	10.36
Orientale	19.4°S	92.8°W	110	11.40
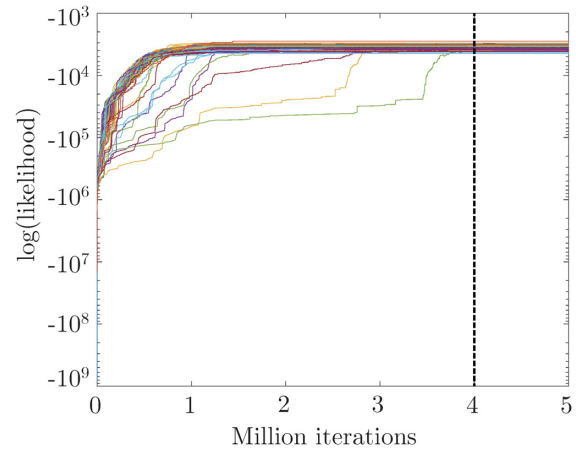
Figure 8. Evolution of the likelihood of models found by each of the 100 independent Markov chains. Each point on represents the likelihood of the density model $\{p_m\}$ accepted at each iteration. As the number of iteration increases, all the chains converge to similar likelihood values. Models after 4 million iterations are regarded as having converged and are sampled (one out of every 1000 model) to form the ensemble used to compute the most likely density model.

were set to $r = 0.99$ and the inner ones to $r = 0.97$. The black circles in Fig. 7 show the outline of these caps and the name of basins on which they are based (Neumann *et al.* 2015). The 2562 acceleration values of this map and the prior probability distributions in Table 1 were the inputs to the inversion. As in the previous test, the prior information was not informative, only limiting the anomalies to be inside the sphere.

3.2.2 McMC set up

One hundred independent Markov chains were run using the gravity acceleration data set of Fig. 7 as input. Each of these chains had a different initial mass distribution model $\{p_m\}$ chosen randomly from the prior distribution. Each chain was run for 5×10^6 iterations of the rjMcMC cycle shown in Fig. 1. Fig. 8 shows that the likelihood of the density models increases with increasing number of iterations. After 4 million iterations, the value of the likelihood no longer changes significantly and is similar for models of all chains. This is taken as a sign of convergence. The ensemble is obtained by sampling one model every 1000 iterations starting after 4 million iterations. Therefore, the ensemble contains 1000 models from each of the 100 chains. The average gravity data produced by this ensemble matches the input gravity data very well with differences of only ± 2 mGal (Fig. 7b).

3.2.3 Fit to target mass distribution

The most likely mass distribution found by the algorithm is obtained by breaking down the volume of the sphere in cells and calculating the average mass from the ensemble in each cell at all depths. This follows from the argument that the models contained in the ensemble are sampled with a frequency representative of the posterior probability. Fig. 9 shows the comparison between the target model and the mean of the ensemble. The output or mean model contains prominent positive masses near the centre of the location of target caps, but they are often surrounded by a ring of negative masses.

(a) Target density distribution

(b) Output mass distribution
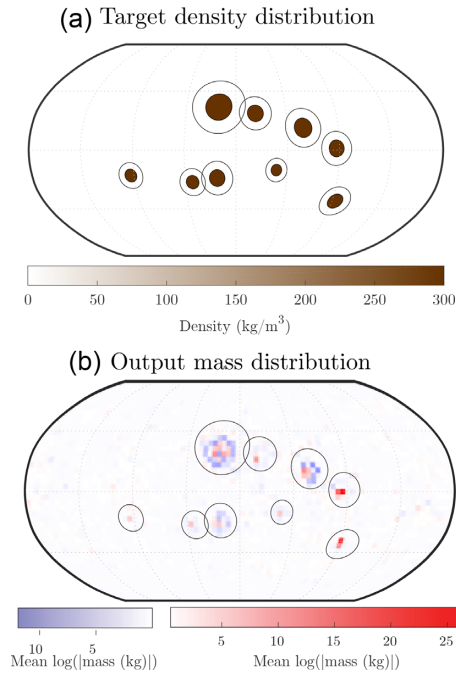
Figure 9. Comparison of the target density model (a) with the location of the point mass anomalies of the mean of the ensemble (b). In map (b), negative anomalies are plotted using the blue colourbar while positive anomalies in the red one. The locations of positive mass anomalies in the output model match the centre of the mascons in the target model. However, their outlines are not perfectly circular and most are surrounded by a ring of negative anomalies. The black circles outline the basins that motivated the density anomalies in the target model; they are shown for reference but are not part of the inversion.

This was not expected since the target model contains only positive density anomalies.

The negative mass anomalies that appear in Fig. 9 could have one of two different origins.

(1) Parsimony of the algorithm encourages the model to match the gravity signature of spherical caps with fewer masses than would be needed to cover the entire spherical cap. Instead of uniformly distributed positive mass anomalies where there is a positive density in the target model, the algorithm uses negative masses to sharpen a broad positive gravity signal. A schematics of this phenomenon is shown in Fig. 10. A well-chosen distribution of positive and negative point masses produces a boxcar-shaped anomaly that resemble the expected signal at the cost of a slightly larger *a posteriori* variance. This interpretation is further supported by a pair of additional synthetic tests we carried out. When inversion is performed on data computed at an elevation of 100 km above the surface, but otherwise identical to those described thus far, the ensemble mass distributions shown in the top panel of Fig. 11 no longer show the rings of negative mass anomalies. This is because the additional distance suppresses high wavenumber features of the mascon gravity data—those arising from the sharp edges shown in Fig. 10—more than the low wavenumber ones corresponding to smooth variations. Similarly, when we increase the maximum allowed value of the noise to 10^{-8}, we allow the inversion to ignore smaller amplitude features, such as those due to the edges; the resulting mass anomalies also no longer show the rings of negative mass, as seen in the bottom panel of Fig. 11.

(2) Since models from consecutive iterations differ from each other only in the location or magnitude of a single anomaly, it is

possible that the algorithm first finds a large, deep positive mass that improves the residual very much. This mass becomes almost impossible to delete because of its effect on the residual and, instead, later models are improved by adding the negative point masses. In essence, the algorithm remains at a local misfit minimum. However, the stochastic acceptance probability adopted in our algorithm and the presence of 100 independent McMC should prevent this kind of effect from dominating the ensemble solution. Therefore, it is most likely that the imperfect distribution of density anomalies returned by our inversion technique is due to the parsimony inherent to THB algorithms.

Another way to compare the inversion result and the target models is to examine the posterior probability distributions computed from the ensemble, which shows the relative frequency of models in the ensemble having certain value of a parameter or a combination of parameters. The credible region of these parameters is calculated as the region where 68 per cent of the posterior probability is located, in a similar fashion than results shown in a 1 σ confidence intervals. Fig. 12 shows the posterior probability of the location of anomalies and their credible region. Peaks of probability match the true location of the centre of mascons, which means that the algorithm effectively recovers the value of these parameters. Fig. 13 shows the posterior probability distribution of mass anomaly depth, $P(\{r\}|\{g\})$. The posterior probably features a marked preference for anomalies at very shallow depth, around the correct depths of $0.97 \leq r \leq 0.99$ which are the same limits the spherical caps in the target model have. This distribution extends deeper than this limits, probably again as a result of the parsimony of the algorithm that can adjust the shape of the gravity anomalies by including deeper point masses (Fig. 10). The credible region is limited by $r \gtrsim 0.87$, which includes the correct value of the target model.

The value of the noise variance is overestimated by the algorithm: $10^{-10} \left(\text{m s}^{-2}\right)^2$ instead of $10^{-11} \left(\text{m s}^{-2}\right)^2$ in the target model. When we repeat the inversion increasing the maximum value of the prior on the noise hyperparameter, the algorithm returns the highest possible value $10^{-8} \left(\text{m s}^{-2}\right)^2$. This implies that the true value of the noise variance is too small to be recovered since it is swamped by the large modelling error of using the point mass parametrization to represent objects of finite size.

The most likely value of the number of anomalies n is 60 with a range between 50 and 73 contained in the 68 per cent credible interval. Although this lacks physical meaning since the true density model is not made of point masses, this shows an important characteristic of the algorithm. The fact that most models have 60 anomalies, less than maximum number allowed (140), shows that the algorithm is indeed parsimonious, as designed. It matches the true gravity data with fewer number of anomalies than the ones it could use.

3.2.4 Uncertainty related to point mass parametrization

In Section 3.2.3 we described how the output mass distribution model or the mean of the ensemble has patterns of negative and positive rings of point mass anomalies where the spherical caps of the target model are located. This shows that using point masses in the THB algorithm contributes to the uncertainty in the interpretation of what the actual internal distribution of the mass in a body is. If the output mass distribution model is given by Fig. 10(c), for example, the actual mass distribution of the interior of the body could be the ones shown in Figs 10(a) or (c). Additional constraints might
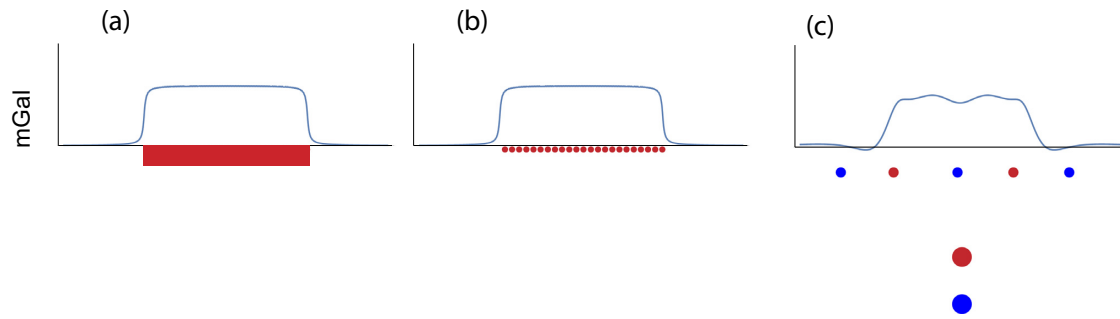
Figure 10. Gravity acceleration produced by different mass distributions. The dots show the location of the point mass anomalies, the size indicates relative magnitude of the mass anomaly, and the colour indicates whether they represent mass surplus (positive mass anomaly, red) or deficit (negative mass anomaly, blue). The blue line shows the values of the gravitational acceleration produced by the point masses. (a) Gravity acceleration produced by the target model which is a density anomaly of finite extent. (b) Gravity acceleration due to many positive point masses can match the gravity acceleration produced by the density anomaly shown in (a). (c) The gravity acceleration in (a) can be approximated with fewer point masses including both positive and negative ones. An inherently parsimonious algorithm would prefer the simpler model comprising fewer point mass anomalies provided that the fit to the data is sufficiently good. This is our explanation for why parsimony can introduce negative mass anomalies into our ensemble solution.
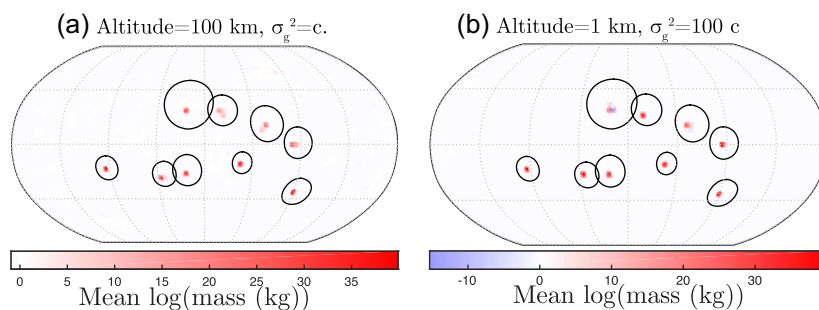
Figure 11. Effect of observation height and noise hyperparameter on retrieval of mass anomalies. Same as Fig. 9 but with (a) synthetic gravity data computed at 100 km elevation above the surface instead of at the surface, and (b) 100 times larger noise variance hyperparameter. Note the disappearance of negative mass rings visible in Fig. 9.

help distinguish between them but, in the absence of such constraints, all these possibilities must be considered. Uncertainty on the inversion results is higher than if instructive *a priori* constraints were used, as in the case where mass anomalies are restricted to a given depth representing, say, the crust–mantle interface. However, in the absence of independent constraints, our approach provides a more complete estimate of the actual uncertainty.

4 DISCUSSION

Most inversions methods that use a spherical harmonic decomposition of the gravity data of a body assume that gravity anomalies are caused by density anomalies as deep as the crust–mantle boundary (Huang & Wieczorek 2012; Wieczorek *et al.* 2013; Jansen *et al.* 2017). These density anomalies are the differences between the expected and actual location of the crust mantle interface. By associating the Bouguer anomaly to the topography of the crust-mantle interface, potential mass anomalies below the core–mantle boundary could be mapped into shallower locations. Other gravity inversion methods allow for variations in the density of the crust or upper mantle but the resulting density anomalies can only be constrained in latitude and longitude and not in depth (James *et al.* 2019). Liang *et al.* (2014) and Zhao *et al.* (2019) find density anomalies correlated to lunar basins down to 100 km but they do not provide the uncertainty of their models or a way to understand how much variation in the resulting density distribution produce the same gravity anomalies. The THB algorithm described here does

not need to assume how deep the mass anomalies are located or if they are all at the same depth. Additionally, the method is parsimonious and introduces only as many mass anomalies as justified by the data. This method yields an ensemble of models that fit the data, which can be analysed to determine the posterior probability density functions describing the latitude, longitude, depth and magnitude of the mass anomalies. The ensemble can be analysed to estimate uncertainty in the inferred mass distributions, including trade-offs between and uncertainties on model parameters due to the inherent non-uniqueness of gravity inversions; this uncertainty covers the range of model parameters that produce a similar fit to the gravity data. Since models are proposed in a random way, and prior information can be incorporated explicitly in a probabilistic way, the results of this method are less likely to be biased.
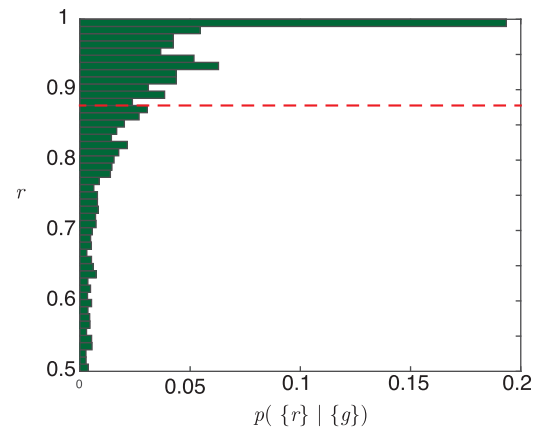
The disadvantages of our THB method compared to the traditional methods based on spherical harmonics inversions is an increase in computational time and memory resources since THB is an iterative method and the ensemble contains many models, each with potentially many parameters to save and analyse. To minimize the computational time and improve efficiency of the model space search, the proposed method is a hybrid one, leveraging linear inversion for point mass anomaly magnitude at each step of the rjMcMC. This reduces the number of iterations needed for convergence and the odds of getting trapped in a local likelihood maxima.

Our validation tests show that while the location of mass anomalies can be readily recovered by the THB method, their detailed shape cannot be confidently estimated when the input gravity data
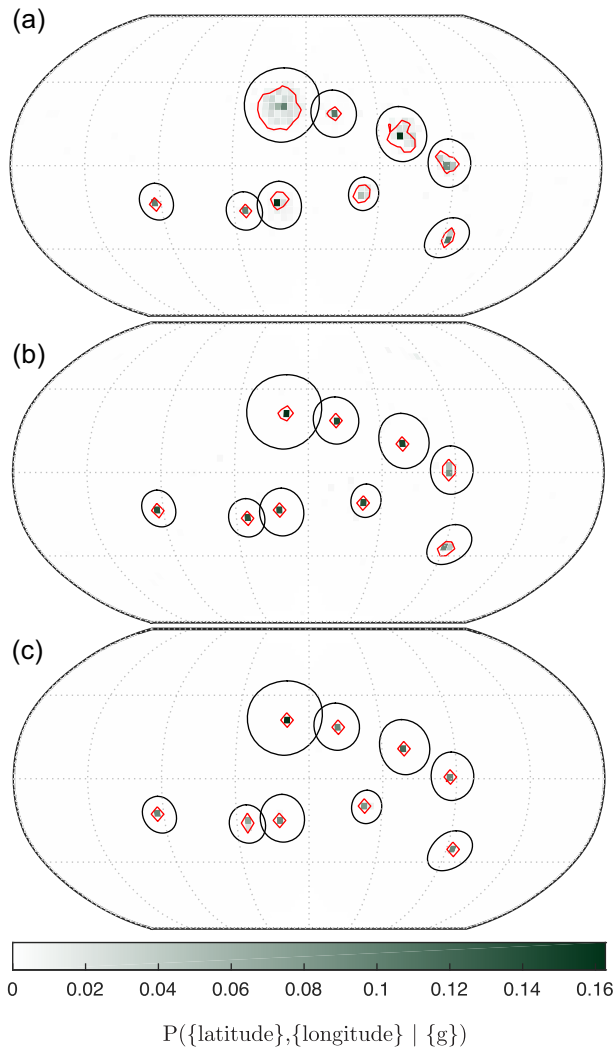
Figure 12. Posterior probability of the latitude and longitude of mass anomalies for three inversions: (a) standard inversion (Figure 8); (b) inversion of the gravity data observed at 100 km height; and (c) inversion with large noise hyperparameter allowed. The red contours outline the regions where the 68 per cent probability region is located. The anomalies are fully contained inside the basins where the target mass anomalies are specified (black circles). Recovery of true centre positions of the input mascons improves when higher altitude gravity observations are used—since they have longer wavelength gravity variations—and when larger noise hyperparameter values are allowed—since they allow the inversion to neglect fitting the sharp corners of the mascon gravity data. 10.

Figure 13. Posterior probability distribution of point mass radius r. The mass anomalies in the target density model have $r = 0.99$ for the outer shell and $r = 0.97$ for the inner shell. The most likely r matches the target value and it is contained in the 68 per cent credible region limited by the red line.

5 CONCLUSION

This study presents a THB algorithm for the inversion of gravity data. This method uses a point mass parametrization, non informative priors, and a larger model space than previous transdimensional Bayesian gravity inversion methods. In order to reduce the number of iterations needed to achieve convergence, an optimization of the magnitude of point masses is applied. A new acceptance probability α that takes into account this optimization is derived.

The performance of the algorithm is assessed through a series of validation inversions which aim to recover a target mass distribution model that contains either point mass anomalies or 3-D objects of constant density anomaly.

The algorithm is able to match perfectly the target model in which the gravity signatures of all point mass anomalies have similar values and are well separated from each other. When the gravity acceleration data is dominated by the signature of fewer point masses than the total number contained in the target model, the algorithm tries to fit only those dominant masses. This is a consequence of parsimony and the transdimensionality of the algorithm. In the second set of inversions, the algorithm finds the correct latitude, longitude and depth of the centre of massive spherical caps but fails to find their outline. Instead the model includes a ring of negative masses and some deeper masses to sharpen the gravity data to better match the the input. For all the tests for which the target model is build from point masses, the algorithm finds the correct noise variance. However, if the target model contains finite size objects, like spherical caps, the variance increases during the inversion above the data uncertainty because of the addition of modelling error arising from the use of point masses and the parsimony of the algorithm. A parametrization based on finite size object such as spherical cap may be better able to recover target models that contain 3-D density objects.

is produced by finite-sized objects. Additionally, we find that the parsimonious nature of the algorithm can cause spurious negative mass anomalies to be introduced into the ensemble solution when the point mass anomaly parametrization is used. We anticipate that both of these drawbacks can be addressed by increasing the complexity of the model parametrization. In particular, we may want to consider a general family of finite size objects instead of just point masses. In that way, it may be possible to infer the location and shape of mascons in the Moon (Neumann *et al.* 2015), Mars (Neumann *et al.* 2004), Mercury (Mazarico *et al.* 2014) and possibly Ceres (Bland *et al.* 2018). However, doing so will come at the price of increased computational costs.

REFERENCES

Anderson, J.D., Jacobson, R.A., Lau, E.L., Moore, W.B. & Schubert, G., 2001. Io's gravity field and interior structure, *J. geophys. Res.,* **106**(E12), 32 963–32 969.

Andrews-Hanna, J.C., 2013. The origin of the non-mare mascon gravity anomalies in lunar basins, *Icarus,* **222**(1), 159–168.

Andrews-Hanna, J.C. *et al.*, 2013. Ancient igneous intrusions and early expansion of the Moon revealed by GRAIL gravity gradiometry, *Science,* **339**(6120), 675–678.

Andrews-Hanna, J.C. *et al.*, 2014. Structure and evolution of the lunar procellarum region as revealed by grail gravity data, *Nature,* **514**, 68–71.

Backus, G.E. & Gilbert, J.F., 1967. Numerical applications of a formalism for geophysical inverse problems, *Geophys. J. Int.,* **13**(1-3), 247–276.

Besserer, J. *et al.*, 2014. GRAIL gravity constraints on the vertical and lateral density structure of the lunar crust, *Geophys. Res. Lett.,* **41**(16), 5771–5777.

Beuthe, M., Maistre, S.L., Rosenblatt, P., Ptzold, M. & Dehant, V., 2012. Density and lithospheric thickness of the Tharsis Province from MEX MaRS and MRO gravity data, *J. geophys. Res.,* **117**(E4), 1–32.

Bland, M.T. *et al.*, 2018. Morphological indicators of a mascon beneath Ceres's largest crater, Kerwan, *Geophys. Res. Lett.,* **45**(3), 1297–1304.

Bodin, T., Sambridge, M., Gallagher, K. & Rawlinson, N., 2012. Transdimensional inversion of receiver functions and surface wave dispersion, *J. geophys. Res.,* **117**(B2), 1–24.

Forte, A. & Peltier, W., 1987. Plate tectonics and aspherical earth structure: the importance of poloidal-toroidal coupling, *J. geophys. Res.,* **92**(B5), 3645–3679.

Gao, C. & Lekić, V., 2018. Consequences of parametrization choices in surface wave inversion: insights from transdimensional Bayesian methods, *Geophys. J. Int.,* **215**(2), 1037–1063.

Genova, A., Goossens, S., Lemoine, F.G., Mazarico, E., Neumann, G.A., Smith, D.E. & Zuber, M.T., 2016. Seasonal and static gravity field of Mars from MGS, Mars Odyssey and MRO radio science, *Icarus,* **272**, 228–245.

Gong, S., Wieczorek, M.A., Nimmo, F., Kiefer, W.S., Head, J.W., Huang, C., Smith, D.E. & Zuber, M.T., 2016. Thicknesses of mare basalts on the Moon from gravity and topography, *J. geophys. Res.,* **121**(5), 854–870.

Goossens, S., Sabaka, T.J., Genova, A., Mazarico, E., Nicholas, J.B. & Neumann, G.A., 2017. Evidence for a low bulk crustal density for Mars from gravity and topography, *Geophys. Res. Lett.,* **44**(15), 7686–7694.

Green, P.J., 1995. Reversible jump Markov Chain Monte Carlo computation and Bayesian model determination, *Biometrika,* **4**, 711–732.

Hager, B.H. & O'Connell, R.J., 1981. A simple global model of plate dynamics and mantle convection, *J. geophys. Res.,* **86**(B6), 4843–4867.

Hastings, W.K., 1970. Monte Carlo sampling methods using Markov chains and their applications, *Biometrika,* **57**(1), 97–109.

Huang, Q. & Wieczorek, M.A., 2012. Density and porosity of the lunar crust from gravity and topography, *J. geophys. Res.,* **117**(E5), doi:10.1029/2012JE004062.

Iess, L., Rappaport, N.J., Jacobson, R.A., Racioppa, P., Stevenson, D.J., Tortora, P., Armstrong, J.W. & Asmar, S.W., 2010. Gravity field, shape, and moment of inertia of Titan, *Science,* **327**(5971), 1367–1369.

Ishii, M. & Tromp, J., 1999. Normal-mode and free-air gravity constraints on lateral variations in velocity and density of Earth's mantle, *Science,* **285**(5431), 1231.

James, P.B., Smith, D.E., Byrne, P.K., Kendall, J.D., Melosh, H.J. & Zuber, M.T., 2019. Deep structure of the lunar south pole-aitken basin, *Geophys. Res. Lett.,* **46**(10), 5100–5106.

Jansen, J. *et al.*, 2017. Small-scale density variations in the lunar crust revealed by GRAIL, *Icarus,* **291**, 107–123.

Koelemeijer, P., Deuss, A. & Ritsema, J., 2017. Density structure of Earth's lowermost mantle from Stoneley mode splitting observations, *Nat. Commun.,* **8**, 1–10.

Konopliv, A. *et al.*, 2014. The Vesta gravity field, spin pole and rotation period, landmark positions, and ephemeris from the Dawn tracking and optical data, *Icarus,* **240**, 103–117.

Konopliv, A. *et al.*, 2018. The Ceres gravity field, spin pole, rotation period and orbit from the Dawn radiometric tracking and optical data, *Icarus,* **299**, 411–429.

Konopliv, A.S. *et al.*, 2013. The JPL lunar gravity field to spherical harmonic degree 660 from the GRAIL Primary Mission, *J. geophys. Res.,* **118**(7), 1415–1434.

Lemoine, F.G. *et al.*, 2013. High degree gravity models from grail primary mission data, *J. geophys. Res.,* **118**(8), 1676–1698.

Li, F., Yan, J., Xu, L., Jin, S., Rodriguez, J.A.P. & Dohm, J.H., 2015. A 10km-resolution synthetic venus gravity field model based on topography, *Icarus,* **247**, 103–111.

Li, Y. & Oldenburg, D.W., 1998. 3-D inversion of gravity data, *Geophysics,* **63**, 109–119.

Liang, Q., Chen, C. & Li, Y., 2014. 3-d inversion of gravity data in spherical coordinates with application to the grail data, *J. geophys. Res.,* **119**(6), 1359–1373.

Lognonné, P., 2005. Planetary seismology, *Ann. Rev. Earth planet. Sci.,* **33**(1), 571–604.

Luo, X., 2010. Constraining the shape of a gravity anomalous body using reversible jump Markov chain Monte Carlo, *Geophys. J. Int.,* **180**, 1067–1079.

Malinverno, A. & Briggs, V.A., 2004. Expanded uncertainty quantification in inverse problems: hierarchical Bayes and empirical Bayes, *Geophysics,* **69**(4), 1005–1016.

Mazarico, E., Genova, A., Goossens, S., Lemoine, F.G., Neumann, G.A., Zuber, M.T., Smith, D.E. & Solomon, S.C., 2014. The gravity field, orientation, and ephemeris of mercury from messenger observations after three years in orbit, *J. geophys. Res.,* **119**(12), 2417–2436.

Melosh, H.J. *et al.*, 2013a. The origin of lunar mascon basins, *Science,* **340**(6140), 1552–1555.

Melosh, H.J. *et al.*, 2013b. The origin of Lunar mascon basins, *Science,* **340**(6140), 1552–1555.

Miljković, K., Wieczorek, M.A., Collins, G.S., Solomon, S.C., Smith, D.E. & Zuber, M.T., 2015. Excavation of the lunar mantle by basin-forming impact events on the moon, *Earth planet. Sci. Lett.,* **409**, 243–251.

Moulik, P. & Ekström, G., 2016. The relationships between large-scale variations in shear velocity, density, and compressional velocity in the earth's mantle, *J. geophys. Res.,* **121**(4), 2737–2771.

Muller, P.M. & Sjogren, W.L., 1968. Mascons: lunar mass concentrations, *Science,* **161**(3842), 680–684.

Neumann, G.A., Zuber, M.T., Smith, D.E. & Lemoine, F.G., 1996. The lunar crust: global structure and signature of major basins, *J. geophys. Res.,* **101**(E7), 16841–16863.

Neumann, G.A., Zuber, M.T., Wieczorek, M.A., McGovern, P.J., Lemoine, F.G. & Smith, D.E., 2004. Crustal structure of Mars from gravity and topography, *J. geophys. Res.,* **109**(E8), doi:10.1029/2004JE002262.

Neumann, G.A. *et al.*, 2015. Lunar impact basins revealed by gravity recovery and interior laboratory measurements, *Sci. Adv.,* **1**(9), doi:10.1126/sciadv.1500852.

Olugboji, T.M., Lekić, V. & McDonough, W., 2017. A statistical assessment of seismic models of the U.S. continental crust using Bayesian inversion of ambient noise surface wave dispersion data, *Tectonics,* **36**(7), 1232–1253.

Romanowicz, B., 2001. Can we resolve 3D density heterogeneity in the lower mantle? *Geophys. Res. Lett.,* **28**(6), 1107–1110.

Sambridge, M., Gallagher, K., Jackson, A. & Rickwood, P., 2006. Transdimensional inverse problems, model comparison and the evidence, *Geophys. J. Int.,* **167**(2), 528–542.

Smith, D.E. *et al.*, 2012. Gravity field and internal structure of Mercury from MESSENGER, *Science,* **336**(6078), 214–217.

Soderblom, J.M. *et al.*, 2016. The fractured Moon: production and saturation of porosity in the lunar highlands from impact cratering, *Geophys. Res. Lett.,* **42**(17), 6939–6944.

Tarantola, A., 2005. *Inverse Problem Theory,* SIAM.

Titus, W.J., Titus, S.J. & Davis, J.R., 2017. A Bayesian approach to modeling 2D gravity data using polygons, *Geophysics,* **82**, 1942–2156.

Wieczorek, M.A. *et al.*, 2013. The crust of the moon as seen by GRAIL, *Science,* **339**(6120), 671–675.

Zhao, G., Chen, B., Uieda, L., Liu, J., Kaban, M., Chen, L. & Guo, R., 2019. Efficient 3D large-scale forward-modeling and inversion of gravitational fields in spherical coordinates with application to lunar mascons.

APPENDIX A: PROPOSAL DISTRIBUTIONS

The general proposal distribution used to generate a new member of the Markov chain Monte Carlo is $q(\{p'_m\}|\{p_m\}) = q(n', \{m'\}, \{x'\}, \{y'\}, \{z'\}, \sigma_g^{2'}|\{n\}, \{m\}, \{x\}, \{y\}, \{z\}, \sigma_g^2)$. As can be seen in Fig. 1, the model $\{p'_m\}$ is chosen by making one of four possible changes in model $\{p_m\}$. Therefore, depending on the change chosen, the proposal distribution simplifies in one of several ways.

(i) Add a new anomaly. The location of the new anomaly is chosen from the prior distribution.

(ii) Change the coordinates of an existing anomaly. This proposal distribution is the same for x, y and z. The magnitude of the standard deviation represents how far or close can be the new location of the anomaly and s is the number of data points in the input gravity data. In the inversions shown in this paper, $\sigma_x = \sigma_y = \sigma_z = 5$ km.

$$q(x'|x) = \frac{1}{\sqrt{\left(2\pi^n\left(\sigma_g^2\right)^s\right)}} \exp\left(-\frac{(x'-x)^2}{2\sigma_x^2}\right) \qquad (A1)$$

(iii) Delete an existing point mass: uniform probability of choosing any of the existing ones.

(iv) Change the variance of noise on input data. The standard deviation of this distribution is $\sigma_{\sigma_g^2}$. For the inversions shown in this paper, $\sigma_{\sigma_g^2} = 4.9 \times 10^{-12}$ $\left(\mathrm{m\ s^{-2}}\right)$.

$$q\left(\sigma_g^{2'}|\sigma_g^2\right) = \frac{1}{\sqrt{\left(2\pi^n\left(\sigma_g^2\right)^s\right)}} \exp\left(-\frac{\left(\sigma_g^{2'}-\sigma_g^2\right)^2}{2\sigma_{\sigma_g^2}^2}\right) \qquad (A2)$$

APPENDIX B: LOCATION OF ANOMALIES OF TARGET MODEL III

The location and magnitude of the anomalies were chosen randomly.

Table B1. Location of anomalies 1–25 of the target model III.

Anomaly	Latitude	Longitude	Radius	Mass (kg)
1	−42.1	−25.9	0.9	7.4879×10^{17}
2	75.3	−58.5	0.49	0.4125×10^{17}
3	−7	11.6	0.94	0.6318×10^{17}
4	66.7	59.1	0.87	0.2002×10^{17}
5	54.9	76.5	0.56	0.3022×10^{17}
6	53.7	52.5	0.62	0.6162×10^{17}
7	−44.1	38.4	0.84	1.9651×10^{17}
8	−21.4	73.5	0.74	0.1294×10^{17}
9	−48.5	−64.8	0.73	4.5031×10^{17}
10	−67.7	41.8	0.82	0.2986×10^{17}
11	60.6	157.5	0.91	3.1491×10^{17}
12	−46.2	123.2	0.85	4.4993×10^{17}
13	22.4	−2.5	0.58	0.2314×10^{17}
14	12.2	170.2	0.87	3.582×10^{17}
15	4.1	−64	0.8	3.0992×10^{17}
16	7.1	−171	0.7	1.9576×10^{17}
17	34.2	26.9	0.89	0.1286×10^{17}
18	−18.4	−92.2	0.9	7.8446×10^{17}
19	−8.4	−20.1	0.8	0.397×10^{17}
20	−39.5	−146.9	0.76	8.8032×10^{17}
21	8.8	−26	0.32	0.1749×10^{17}
22	−40.9	173.5	0.75	0.9531×10^{17}
23	38.8	−14.5	0.65	0.4445×10^{17}
24	−35.8	−169.8	0.99	5.0659×10^{17}
25	48.1	117.6	0.76	0.4204×10^{17}

Table B2. Location of anomalies 26–50 of the target model III.

Anomaly	Latitude	Longitude	Radius	Mass (kg)
26	12	−37	0.71	2.0249×10^{17}
27	−16.7	−0.5	0.63	4.1305×10^{17}
28	16.5	128	0.59	8.5556×10^{17}
29	−61.2	50.9	0.59	3.3633×10^{17}
30	−46.9	−131.1	0.79	0.1691×10^{17}
31	−70.3	177.2	0.71	1.3994×10^{17}
32	29.8	−179.1	0.91	0.4983×10^{17}
33	−11.1	53.5	0.77	0.8389×10^{17}
34	−39.6	35.5	0.89	8.8763×10^{17}
35	36.9	−34.5	0.44	0.1471×10^{17}
36	11.7	91.4	0.65	0.3964×10^{17}
37	16.7	−93.4	0.49	0.7331×10^{17}
38	−9.1	−116.2	0.67	0.2973×10^{17}
39	4.9	−30.6	0.73	0.9013×10^{17}
40	−39.3	−119.2	0.8	3.9532×10^{17}
41	38.7	−100.3	0.92	1.3488×10^{17}
42	−38.8	97.3	0.87	1.0252×10^{17}
43	−31.1	−19.7	0.93	2.4992×10^{17}
44	−37.4	57.8	0.75	1.1489×10^{17}
45	−52.9	−24.8	0.68	0.3238×10^{17}
46	17.9	179.7	0.79	0.2273×10^{17}
47	−10.9	−115	0.86	1.33×10^{17}
48	24.3	93	0.29	0.6577×10^{17}
49	55.5	128.7	0.23	0.7973×10^{17}
50	−26.1	105.1	0.65	2.4374×10^{17}